Dielectric relaxation analysis of Pb(Zr0.54,Ti0.46)O3 thin films: electric field dependence

Freddy Ponchel, N. Sama, Denis Remiens, T. Lasri

Journal of Applied Physics

Dielectric relaxation analysis of $Pb(Zr_{0.54},Ti_{0.46})O_3$ thin films: Electric field dependence

Cite as: J. Appl. Phys. **116**, 244108 (2014); https://doi.org/10.1063/1.4904514
Submitted: 27 August 2014 • Accepted: 07 December 2014 • Published Online: 29 December 2014

F. Ponchel, N. Sama, D. Rémiens, et al.

JOURNAL OF APPLIED PHYSICS **116**, 244108 (2014)

Dielectric relaxation analysis of $Pb(Zr_{0.54},Ti_{0.46})O_3$ thin films: Electric field dependence

F. Ponchel,[1,a)] N. Sama,[3] D. Rémiens,[1] and T. Lasri[2]
[1]*Institute of Electronics, Microelectronics and Nanotechnology (IEMN), UMR CNRS 8520, DOAE Department, University of Valenciennes et du Hainaut Cambresis, Le Mont Houy, 59313 Valenciennes Cedex 9, France*
[2]*Institute of Electronics, Microelectronics and Nanotechnology (IEMN), UMR CNRS 8520, DHS Department, University of Lille1 Sciences and Technologies, 59652 Villeneuve d'Ascq Cedex, France*
[3]*Institut National de la Recherche Scientifique - Energie Matériaux et Télécommunications (INRS-EMT), 10 1650 Boulevard Lionel Boulet, Varennes, Quebec J3X 1S2, Canada*

(Received 27 August 2014; accepted 7 December 2014; published online 29 December 2014)

350 nm-thick Perovskite $PbZr_{0.54}Ti_{0.46}O_3$ (PZT) thin films were deposited on Al_2O_3 substrates by sputtering with and without an additional 10-nm-thick TiO_x buffer layer. X-ray diffraction patterns showed that in presence of TiO_x buffer layer, PZT film was highly oriented along the (111) direction film, whereas the unbuffered, counterpart was polycrystalline. A full wave electromagnetic analysis using a vector finite element method was performed to determine the tunability and the complex permittivity up to 67 GHz. A comparison between the electromagnetic analysis and *Cole-Cole* relaxation model was proposed. Through an original study of the relaxation time as a function of the electric field, values, such as 2 ps and 0.6 ps, were estimated for $E_{DC} = 0$ kV/cm and 235 kV/cm, respectively, and in both cases (111)-PZT and polycrystalline-PZT. The distribution of relaxation times is found to be larger for (111)-PZT film, which is probably related to the film microstructure. © *2014 AIP Publishing LLC*. [http://dx.doi.org/10.1063/1.4904514]

I. INTRODUCTION

Perovskite structure-type oxides exhibit a wide range of functionality owing to their outstanding ferroelectric, piezoelectric, and pyroelectric properties.[1–4] Since several years, the development of ferroelectric thin films of high quality, such as $Pb(Zr,Ti)O_3$ (PZT), $SrBi_2Ta_2O_9$ (SBT), and $(Ba,Sr)TiO_3$ (BST), has allowed the integration of ferroelectric-based devices in microelectronics for different kinds of applications. For example, BST has stimulated considerable efforts in designing microwave electric field-agile devices without resorting to active components.[5–7] Likewise, PZT plays an important role in piezo-MicroElectroMechanical Systems (PiezoMEMS), such as actuators/micro-sensors and also in non-volatile memory applications, such as ferroelectric random access memory (FRAM), where the storage data cells are obtained by means of PZT-based capacitors.[8,9] So, one can say that in recent years, studies have been mainly dedicated to the development of devices. Many theoretical investigations have been achieved to explain some specific behaviour observed in thin film form, such as fatigue or domain switching, as for example, for memory applications. But a limited number of works about the relaxation time of ferroelectric materials in thin film form have been published except studies concerning the temperature effect on the dielectric relaxation. In bulk form (ceramic), the dielectric response of ferroelectric materials has attracted much more attention in the past, in particular, because of their interesting dielectric relaxation properties. It is well known that for this kind of materials, the dielectric relaxation mechanisms are very sensitive to parameters, such as temperature, electric field, structural, and micro structural aspects (defects, grain size, charge carriers…).[10–13] To describe the behaviour of such materials, relaxation models have been developed and among them, the Debye's model was the first one proposed to evaluate the dielectric behaviour by using a single relaxation time approach.[14] Then this model has been modified by introducing a correction factor considering a distribution of relaxation times to obtain the Cole-Cole's model.[15]

In this study, our work is focused on ferroelectric oxides that present a perovskite structure. PZT material with a composition near the morphotropic zone was chosen for the experiments. We were interested in PZT because its level of losses is sufficient to perform a characterization in a large frequency range. In the study, the frequency band selected spans from 1 GHz to 67 GHz. It should be mentioned that we have already qualified BST thin films in terms of permittivity and tunability at microwave frequencies.[16–18] So it would have been interesting to complete the dielectric characterizations by studying the relaxation time. Nevertheless, given the low level of losses in the case of BST, frequencies in the range of several hundred of GHz would have been required (about 800 GHz) to make the relaxation time measurable. Taking into account this constraint, and in order to demonstrate the performance of the method we developed, we propose in this paper a complete characterization of polycrystalline and (111)-oriented PZT films, namely, permittivity, tunability, and loss angle up to 67 GHz. The retrieval of the dielectric properties from S-parameters measurements is based on a full wave 2D-vector finite element method. The results of extraction and the measurement of the dielectric infinite permittivity (ε_∞) together with a

a)Author to whom correspondence should be addressed. Electronic mail: freddy.ponchel@univ-valenciennes.fr

Cole-Cole approach are then used to estimate the characteristic relaxation time of the thin film as a function of the applied electric field.

II. PZT PREPARATION AND STRUCTRAL ANALYSIS

PZT films were deposited on (0001) Al_2O_3 substrate by RF-magnetron sputtering. In order to estimate the influence of the crystallographic orientation on the dielectric properties, two PZT films with different crystallographic orientations were fabricated. Previous studies have already shown that the introduction of a TiO_x buffer layer could enhance the (111)-orientation of PZT films.[19,20] In this study, the idea was to make use of this experience, thus on the one hand, a 10 nm-thick TiO_x buffer layer was sputter-deposited on Al_2O_3 substrate before depositing the $PbZr_{0.54}Ti_{0.46}O_3$ thin film. On the other hand, no buffer layer was inserted between the Al_2O_3 substrate and the $PbZr_{0.54}Ti_{0.46}O_3$ layer. After deposition of the TiO_x buffer layer onto Al_2O_3 substrate and before deposition of PZT, the TiO_x/Al_2O_3 sample was annealed at 700 °C in air, the objective of this treatment was to bring the degree of oxidation of the TiO_x film at or close to its stoichiometric value: x = 2. Table I summarizes the sputtering conditions used to simultaneously fabricate PZT/Al_2O_3 and PZT/TiO_x/Al_2O_3 structures.

The as-deposited PZT films were amorphous because substrates were not heated during deposition. So after deposition, the films were post-annealed at 625 °C during 30 min for crystallization in perovskite phase.[21] The thickness of both PZT films, measured thanks to a Veeco Dektak 150 profilometer, was 350 nm. Structural analyses were performed through X-ray diffraction (XRD) using a Siemens D5000 diffractometer with filtered Cu Kα1 radiation ($\lambda = 1.5406$ Å). Figure 1 shows the X-ray diffraction diagrams of the PZT films. The θ-2θ scan covered the range 20°–60° with steps size of 0.02°.

It is clearly observed (Figure 1) that the PZT film deposited directly on Al_2O_3 (black line) was polycrystalline, whereas the one deposited on TiO_x/Al_2O_3 (blue line) was oriented along the (111) axis. These results are in perfect agreement with the literature.

III. MICROWAVE MEASUREMENTS AND DIELECTRIC PROPERTIES EXTRACTION

The method used to determine the dielectric properties (relative permittivity, loss factor, and tunability) of PZT in the high-frequency domain is based on the fabrication of microgap coplanar waveguides (M-CPW) deposited directly on the material to be tested. The microgaps were obtained by 365 nm UV photolithography using a negative imaging photoresist. The thickness of the photoresists layer was 800 nm, the exposure energy was 38 mJ/cm^2, and no adhesion promoter was necessary on the PZT samples. The planar electrodes consisting of a 50 nm Ti adhesion layer and 450 nm Au layer were obtained by evaporation process. Figure 2 shows a scanning electron microscope (SEM) view of one of the realized coplanar waveguides (top view, zoomed top view, and cross section view). The cross section view reveals that the thin film is not fully dense (presence of porosity observed on the two samples: PZT/Al_2O_3 and PZT/TiO_x/Al_2O_3). This porosity effect on the effective permittivity has been investigated and different numerical methods and analytical models have been proposed in the literature.[22] Although our study was not focused on this effect, we believe that the final result of the permittivity modulus $|\varepsilon^*|$ is potentially lower than that of a fully dense PZT. Nevertheless, according to the literature, we can estimate that the extracted thin film permittivity modulus $|\varepsilon^*|$ represents more than 90% of a fully dense PZT. Note that the porosity has no impact on the ratio $\varepsilon''/\varepsilon'$ and the relaxation parameters.

The optical masks used during exposure include several hundred of M-CPWs collected in sets of 10 pieces. Within

TABLE I. Sputtering parameters used for TiO_x and PZT layers.

	TiO_x deposition parameters	PZT deposition parameters
Target composition		PZT 54/46
Target diameter	152.4 mm (6")	76.2 mm (3")
Distance target-substrate	50 mm	60 mm
Gas	Argon + O_2	Argon
Pressure	2×10^{-2} mbar	10^{-2} mbar
RF power	1.6 W/cm^2	2.36 W/cm^2
Substrates	Al_2O_3	Al_2O_3 and TiO_x/Al_2O_3

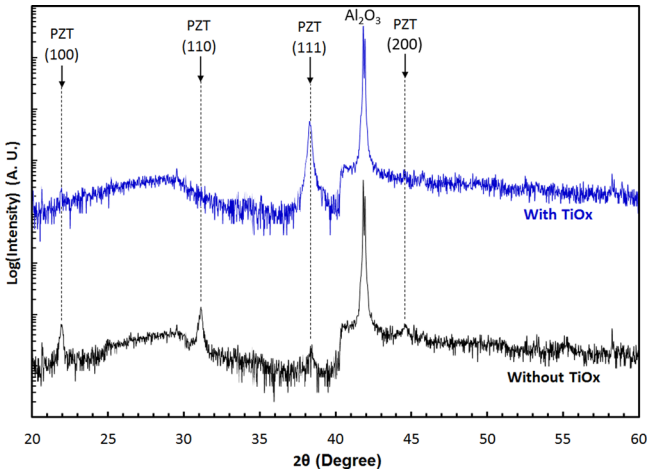

FIG. 1. X-ray diffraction patterns of 350 nm-thick $PbZr_{0.54}Ti_{0.46}O_3$ films deposited on Al_2O_3 substrate annealed at 625 °C during 30 min. Black line: PZT without a TiO_2 buffer layer. Blue line: PZT with a TiO_2 buffer layer.

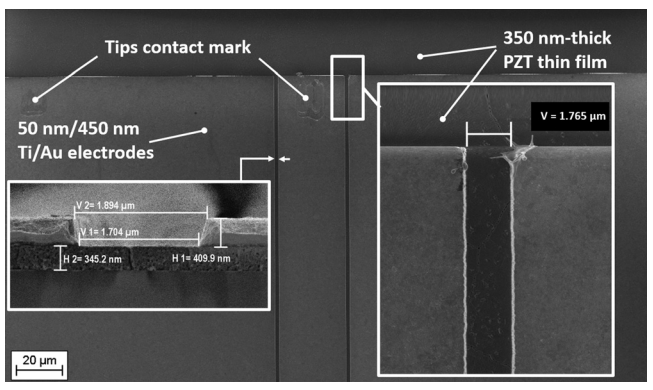

FIG. 2. SEM view (top and cross section) of the 1.7 μm slot width coplanar waveguide. The total length of the structure is 3 mm.

the same group, the microgap slots present different widths (from 1 μm to 2 μm with steps of 0.2 μm and from 2 μm up to 4 μm with steps of 0.5 μm). This allows adjusting the effective permittivity of the structure (depending on the relative permittivity of the material under test and its thickness) and consequently leads to the best design that takes into account both frequency and biasing (V_{DC}) criteria. All other dimensions of M-CPWs were fixed; the central conductor width was set to 30 μm, the ground plane's width is adjusted to 190 μm, and the total length of each M-CPW is chosen to be equal to 3 mm. One can note that the smallest achievable gap by using UV-360 nm optical lithography to fabricate CPW was 1 μm. So, beyond this limit, it is necessary to switch to electron beam lithography.

Microwave measurements were carried out at room-temperature (22 °C) using an Agilent E8361A Precision Network Analyzer (PNA) coupled to a Cascade Microtech ground-signal-ground probe station. The scattering parameters were measured in the frequency range 1–67 GHz for a −10 dBm input power. Given the remarkable stability and reproducibility of the measurements, no averaging was applied. Each measurement was performed with an intermediate frequency bandwidth of 10 Hz in order to have a maximum dynamic range and a minimum uncertainty on the transmission and reflection coefficients (uncertainty less than 0.2 dB for a dynamic range between 0 and −35 dB). These measurement characteristics result in a relative uncertainty of approximately 2% on the final results. For DC electric field control, an Agilent E5263A 2-Channel High Speed Source Monitor Unit was used. The measurement station set is driven by IC-CAP device modeling software v2009. For each tested coplanar structure, the characterization protocol consisted in measuring the S-parameters for 41 bias voltage points following the sequence 0 → 40V → 0 → −40 V → 0 (if $|V_{DC}| < 10$ V, the step is 2.5 V, if $|V_{DC}| > 10$ V, the step is 5 V). Note that this value of 40 V corresponds to the maximum voltage possible with the internal PNA bias tee. Finally, the experimental reference planes for wave port 1 and wave port 2 are determined using a SEM photograph of the G-S-G tips marks on the gold electrodes (Fig. 2). The distance between the marks and the edge of the central line (for wave port 1 and wave port 2) is measured for each tested coplanar structure and taken into account in our home made software.

It should be mentioned that a complete study was carried out for the considered structures, namely, polycrystalline and (111)-oriented PZT films. Indeed, characteristics of interest, such as permittivity, tunability, and loss angle, were investigated in a large frequency range, up to 67 GHz, in both cases. For readability, we have chosen to present the whole development of the method for only one situation, the (111)-oriented PZT films. Nevertheless, for comparison purpose, the *Cole-Cole* parameters extracted for polycrystalline and (111)-oriented PZT films are summarized at the end of the paper.

Figure 3 shows the S-parameters measured for the 11 first V_{DC} points (from 0 V up to 40 V). Figure 3(a) reports the reflection coefficient on wave port 1, S_{11} measured on the (111)-PZT sample from a 1.7 μm slot width M-CPW (identical results were obtained on polycrystalline film). The reflection coefficient on port 2 (not represented here) was strictly the same. Note that the examination of the difference between S_{11} and S_{22} is a good way to verify if the layer below the M-CPW has a constant thickness. The selection of

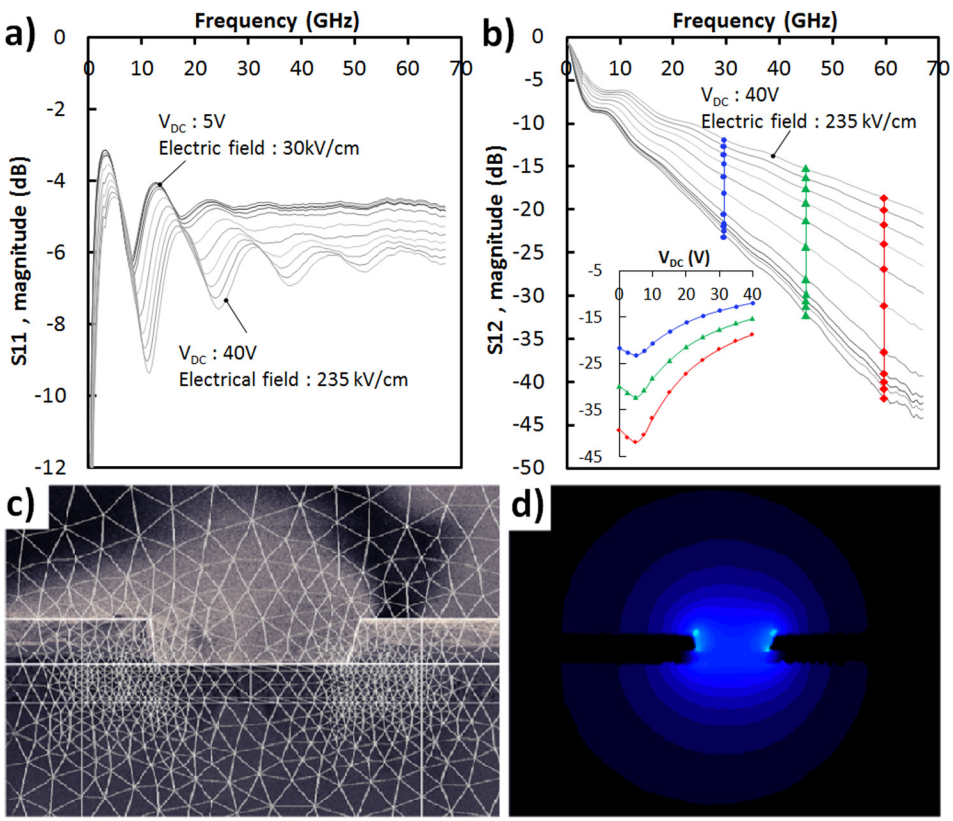

FIG. 3. (a) Frequency dependence until 67 GHz of the reflected S-parameter (a) and transmitted S-parameter (b) for V_{DC} from 0 V up to 40 V (if $|V_{DC}| < 10$ V, the step is 2.5 V, if $|V_{DC}| > 10$ V, the step is 5 V). (c) Meshed SEM view used for the PZT complex permittivity extraction. (d) Confined electric field solution taken during the computational phase in one CPW-slot.

the devices was made on this basis. A few key points should be considered in interpreting these results. S_{ii} ($i = 1, 2$) is the sum of two independent contributions. First, the average value $\langle S_{ii}(f) \rangle$ that reveals the impedance mismatch between the device under test and the reference impedance of the measurement system ($Z_{ref} = 50\ \Omega$) which is a quasi-constant on all the frequency range. For $V_{DC} = 0$ V up to 40 V, $\langle S_{ii}(f) \rangle$ evolved from -4.7 dB to -6.5 dB, the corresponding characteristic impedances are approximately 14 Ω and 17 Ω, respectively. The second point to be considered is the oscillating phenomenon due to the proximity of the second wave port. Indeed, the waveguide boundaries may be seen as a partially reflecting mirror like in a Perot-Fabry photonic cavity. The magnitudes and the broadenings of these oscillations grow with increasing V_{DC}. Thus, with increasing V_{DC}, effective permittivity decreases implying a reduction in the total losses and the electrical length of the waveguide. Figure 3(b) shows the S_{ij}-parameters ($i = 1, 2, j = 1, 2, i \neq j$), i.e., the total insertion loss into the device. The inset in Figure 3(b) exhibits the V_{DC} dependence of S_{ij}-parameters at 30 (blue line), 45 (green), and 60 GHz (red). It illustrates the impact of the material on the wave behavior. Indeed, this underlines the hysteresis loop that characterizes a ferroelectric phase material.

The S-parameters were measured using a 1.7 μm M-CPW but this dimension is not actually the optimal one to obtain a maximum electrostatic field and consequently, a maximum dynamics for the tunability measurement. However, it permits to obtain acceptable S_{ij}-parameters up to 67 GHz. For example, in these conditions, S_{12} reached -45 dB at 67 GHz. Admittedly, this value is extremely low and close to the limits of the PNA. Actually, among all the measurements on different slot widths (1 μm up to 4 μm), this result was the best compromise between frequency dependence and V_{DC} dependence. Under these conditions ($V_{DC} = 40$ V, slot width $= 1.7\ \mu$m), the maximum electrostatic field inside the thin film was $E_{DC} = 235$ kV/cm.

From these measured S-parameters and the precise geometrical characteristics obtained through SEM imaging, the dielectric characteristics were extracted by a full wave electromagnetic analysis. We make use of a homemade software based on a two-dimensional vector finite element method especially developed for microwave characterizations of materials. Special care is given to the mesh operation which is adjusted from a mapping process directly on the SEM picture (see Figure 3(c)). Figure 3(d) shows the confinement of the transverse electric field at 10 GHz. Note that with this electrode topology, the electric field in the thin film is located only in the 1.7 μm-microgap spacing. Compared to M-F-M (Metal/Ferroelectric/Metal) structure, where the electric field is below the metallic electrodes, a planar propagation device is more convenient because it is less sensitive to parasitic effects, in particular, to the Schottky effect on the apparent permittivity with respect to the film thickness as described in Ref. 23. In the following results, we do not represent error bars mainly for readability reasons and we prefer to point out here that all results have a relative uncertainty of less than 2% (including measurement uncertainty and computational errors in numerical analysis).

The inversion-based computational procedure provided complex permittivity $\varepsilon^* = \varepsilon' - j\varepsilon''$ of the PZT layer from the S-parameters measurement for each frequency point and each DC applied voltage point. Figure 4(a) represents the frequency dependence of the complex permittivity for the 11 first DC applied voltages, i.e., from 0 V up to 40 V corresponding to electric field of 0 kV/cm and 235 kV/cm, respectively, into the 1.7 μm-coplanar slot. These results were then interpolated by using the *Cole-Cole* function and plotted in Figure 4(b) as a function of frequency. The inset (Figure 4(c)) shows the same information in a ε''-ε' graph. A description

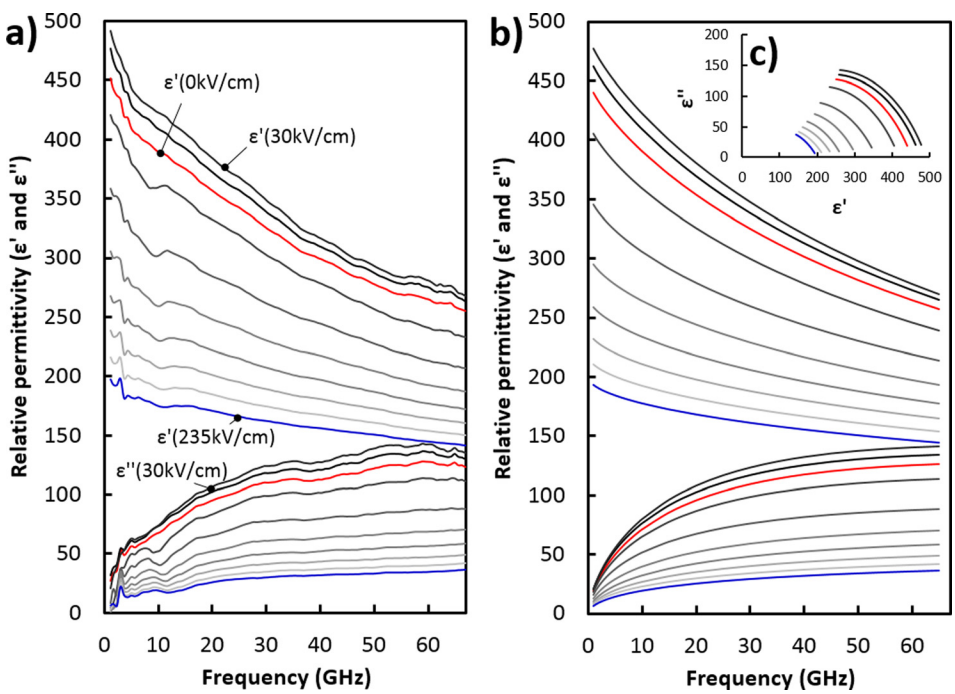

FIG. 4. (a) Frequency behaviour of the complex permittivity ($\varepsilon^* = \varepsilon' - j\varepsilon''$) of a 350 nm-thick PZT layer deposited on Al_2O_3 substrate. These values have been computed by 2D Full-wave electromagnetic field simulator (home made) from 401 [S] parameter measurement points and for each frequency points, 41 bias voltage points following the sequence 0→40→0→−40→0. (b): Interpolation of the PZT complex permittivity results in (a) using the *Cole-Cole* function and a method described in Sec. III. The inset (c) present the *Cole-Cole* interpolation in a ε''- ε' graph.

of the method used to achieve this *Cole-Cole* fitting is detailed in Sec. IV. From both Figures 4(a) and 4(b), it can be seen that whatever the external electric field, the real part of the relative permittivity (ε') is continuously diminishing with a very important slope. At 0 kV/cm for instance, ε' has a value of 452 at 1 GHz, 408 at 5 GHz, and drops to 255 at 67 GHz (red curve on Figures 4(a) and 4(b)). This corresponds in average to a 44% relative dispersion on the complete frequency band (≈0.67%/GHz). The maximum decreasing (0.7%/GHz) was observed for the maximum modulus of complex permittivity which corresponds, for this PZT thin film, to an applied electric field of 30 kV/cm. At 235 kV/cm, ε' has a value of 197 at 1 GHz, 182 at 5 GHz, and 141 at 67 GHz, and the relative dispersion is about 28% (≈0.4%/GHz). As a comparison, in previous studies, for example, in the case of the characterization of BST thin films, we have obtained a maximum of 5% relative dispersion on the same frequency band (0.08%/GHz).[16] Of course, this very high dispersion is directly related to the dielectric losses. Indeed, the dielectric losses that we display in terms of loss tangent ($\tan\delta = \varepsilon''/\varepsilon'$) exceed 50% in the worst case. Again, the maximum losses are obtained for an applied electric field of 30 kV/cm.

We present the behavior of the relative permittivity (Fig. 5(a)) and the loss tangent (Fig. 5(b)) as a function of E_{DC} at 1 GHz, 5 GHz, and 67 GHz. The tunability is defined as $\{(max(\varepsilon')–min(\varepsilon'))/max(\varepsilon')\} \times 100$ (in %). In the present case, the maximum and minimum permittivities correspond to applied electric fields of 30 kV/cm and 235 kV/cm, respectively. As we can observe in the table included in Figure 5(a), the tunability is close to 60% up to 5 GHz and about 47% at 67 GHz. This behavior is directly related to the DC field dependence of the dispersion as pointed out above (0.7%/GHz at 30 kV/cm, 0.4%/GHz at 235 kV/cm).

IV. *COLE-COLE* MODEL FITTING: RELAXATION TIME ESTIMATION

In the results presented in Figure 4(a), the level of losses at 67 GHz suggests that we should be close to the characteristic relaxation time of the PZT thin film. It is of interest to relate these experimental data with a physical relaxation model in order to estimate this characteristic relaxation time. An initial analysis was investigated using the Debye model. However, in the results presented in Figure 4 (for example, the curve ε' (30 kV/cm)), the variation of ε' observed for the lowest frequencies (typically between 1 GHz and 10 GHz) indicates that Debye relaxation model is not sufficient. For example, the differentiation, with respect to ω $d\varepsilon'_{Debye}/d\omega$ approaches 0 when ω approaches 0 and this is not consistent with our results ($d\varepsilon'_{Measure}/d\omega < 0$ in our case). The results presented by Hassen *et al.*[12] (notably Figure 4) are a good illustration of these remarks. Indeed, it was well established that the Debye expression with a single relaxation time cannot describe the dielectric response of the majority of complex systems (complex microstructures, presence of grain boundaries, and different grain sizes/orientations). In order to better explain the experimental observations, we make use of the Cole-Cole's model that allows describing a spectral distribution of relaxation times thanks to an additional parameter α. We note $\varepsilon^*_{C\text{-}C}$ this complex permittivity

$$\varepsilon^*_{C-C}(\omega,\theta) = \varepsilon'_{C-C}(\omega,\theta) - j\varepsilon''_{C-C}(\omega,\theta) = \varepsilon_\infty + \frac{\varepsilon_S - \varepsilon_\infty}{1 + (j\omega\tau)^\alpha}, \tag{1}$$

$\theta = (\varepsilon_S, \varepsilon_\infty, \tau, \alpha)$ is a set of parameters. ε_S and ε_∞ are, respectively, the static and optic dielectric permittivity. The parameter τ is the central value of the symmetric spectral distribution of relaxation times and α characterizes the broadening of this distribution. In this formula, α must be

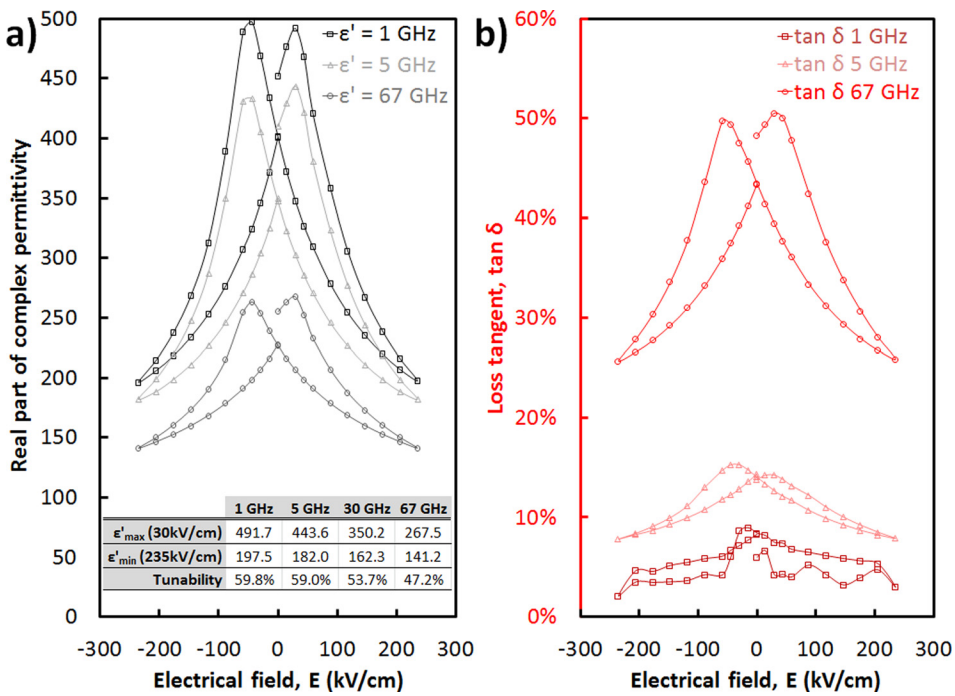

FIG. 5. Real part of relative permittivity (a) and loss tangent (b) versus E_{DC} (the electrical applied field) measured for $F = 1$, 5, and 67 GHz.

between 0 and 1. If $\alpha = 1$, expression (1) corresponds to the Debye model with a single relaxation behavior. The case $\alpha = 0$ represents an infinitely broad and continuous distribution. Note that for a particular value of τ, there is a particular peak loss frequency $f_{peak} = (2\pi\tau)^{-1}$ for which ε'' passes through a maximum.

The purpose of the computational method developed is to fit the *Cole-Cole* parameters θ to the experimental data. To that end, an algorithm based on the least squares method was implemented in Matlab environment. In the least-squares sense, the best solution minimizes the squared sum of the scalar residue $\boldsymbol{F_n}(\theta)$. In our case, the total residue at the i-th iteration can be described by the following expression:

$$F_i(\theta_i) = \sum_{n=1}^{N} F_n(\theta) = \sum_{n=1}^{N} |\varepsilon^*_{meas}(\omega_n, V_{DC}) - \varepsilon^*_{C-C}(\omega_n, \theta_i)|^2, \tag{2}$$

where $\varepsilon^*_{meas}(\omega_n, V_{bias})$ represents the experimental data presented in Figure 4, N is the total number of measured frequency points provided by the network analyzer. For any value of n, $F_n(\theta)$ represents the error between the observed value $\varepsilon^*_{meas}(\omega_n, V_{DC})$ and the fitted value $\varepsilon^*_{C-C}(\omega_n, \theta)$ provided by expression (1).

In this algorithm, each parameter θ is a random variable taken in the closed interval $[\theta_a, \theta_b]$, where θ_a and θ_b ($\theta_a < \theta_b$) are real values defined beforehand. Note that the length of the segment $[\theta_a, \theta_b]$ can be reduced under certain conditions tested during the calculation phase. This obviously leads to a significant performance increase. Thus, for the i-th iteration, a new set of parameter θ_i is drawn lots and a new residue $\boldsymbol{F_i}(\theta_i)$ is computed. If $\boldsymbol{F_i}(\theta_i)$ is greater than a reference value, nothing happens, and the algorithm goes to the next iteration. On the contrary, if $\boldsymbol{F_i}(\theta_i)$ is smaller than the reference value, then $\boldsymbol{F_i}(\theta_i)$ becomes the new reference. Of course, in this last condition, the corresponding set θ_i is saved. A validation phase was carried out to evaluate the fit quality as a function of the iteration number N_i. This study shows that in this situation where four random variables are present, $\boldsymbol{F_i}(\theta)$ is constant for $N_i \geq 5 \times 10^3$ for any V_{DC}. Of course, the value of this constant is directly related to the noise measurement. This simple approach based on the least squares method coupled to a dynamic interval of random variable is the basis of a reliable and efficient tool to fit experimental data.

An interval for most of *Cole-Cole* parameters can be derived directly from measurements except for the optical dielectric permittivity ε_∞. In order to obtain an experimental interval for ε_∞, the elliptic constants of the PZT thin film were measured by using spectroscopic phase modulated ellipsometer. Preliminarily, a chemical etching using a 36% hydrochloric acid solution was carried out to remove PZT at an edge of the sample and allowed obtaining the elliptic response of Al_2O_3 substrate only. The measurements were performed at room-temperature (22 °C like for microwave measurements) using a Horiba Jobin Yvon instrument and DeltaPsi2 software. The photon energy region is from 0.75 to 4.75 eV by step of 0.02 eV with an incident beam angle of 60°. The results of the complex optical index are given on Figure 6(b) for Al_2O_3 substrate only and for PZT onto Al_2O_3.

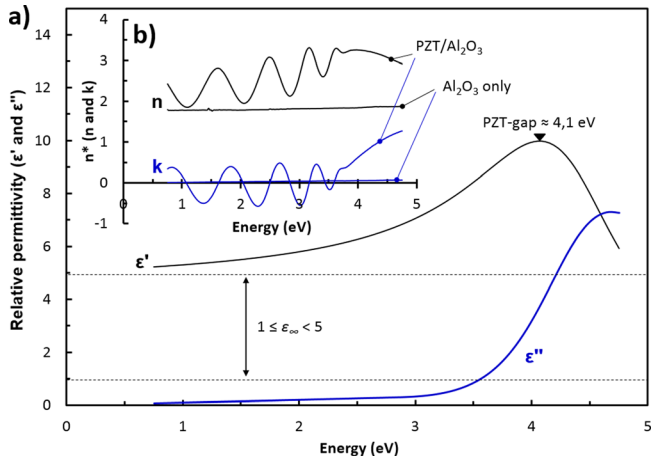

FIG. 6. Dielectric function of the PZT layers (a) and refractive index function measured on Al_2O_3 substrate and (111)-PZT/Al_2O_3 sample in the spectral range of 0.75–4.75 eV.

In the investigated zone, the PZT thin film has a thickness of 300 nm (profilometer measurement). All these data allowed extracting the complex index of PZT layers. Many dispersion models offered by the DeltaPsi2 software were compared and the best matching was obtained by using the Adachi-New Forouhi model. The result is presented Figure 6(a) in terms of complex permittivity versus frequency. This experiment also allowed defining an experimental interval for optic dielectric permittivity ε_∞. The photon energy region used here has brought out the photonic gap of our PZT thin film which is estimated here at 4.1 eV, a value close to the result of Lee *et al.*[24] This value is the same whatever the crystallographic orientation of the film.

Finally, the algorithm was initialized with a fixed interval wide enough to include all the experimental data of

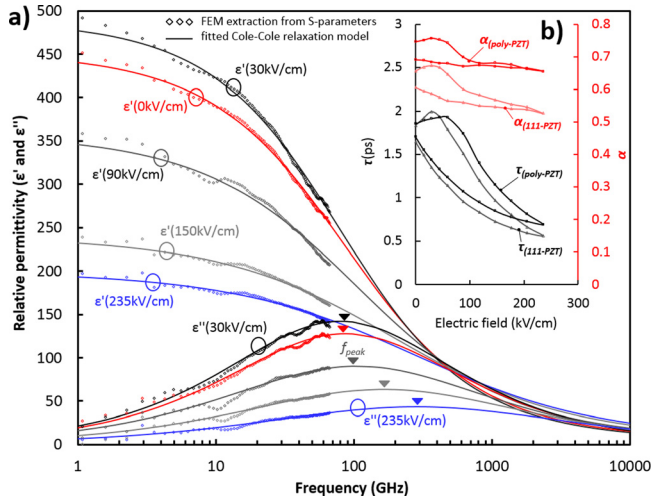

FIG. 7. (a) Comparison between FEM direct-extraction from S-parameters (dotted lines) and fitted *Cole-Cole* relaxation model (continuous lines) on a large frequency logarithmic-scale obtained on the (111)-PZT sample. (b) *Cole-Cole* parameters (τ: the central relaxation time and α: the distribution broadening) obtained on the two samples: (111)-PZT and polycrystalline-PZT.

TABLE II. Synthesis of *Cole-Cole* fitted parameters.

	ε_S		ε_∞		τ (ps)		$(2\pi\tau)^{-1}$ (GHz)		α	
E_{DC} (kV/cm)	(111)	poly	(111)	poly	(111)	poly	(111)	poly	(111)	poly
0	453.80	395.69	4.59	4.86	1.84	1.85	86.63	85.89	0.66	0.75
30	490.67	406.02	4.60	4.97	1.99	1.91	79.74	83.16	0.67	0.76
88	358.91	350.32	4.81	4.82	1.51	1.74	105.35	91.49	0.60	0.70
147	268.37	245.97	4.96	4.92	0.97	1.15	164.04	138.41	0.57	0.68
235	199.15	171.86	4.96	4.85	0.56	0.69	283.26	229.64	0.53	0.65

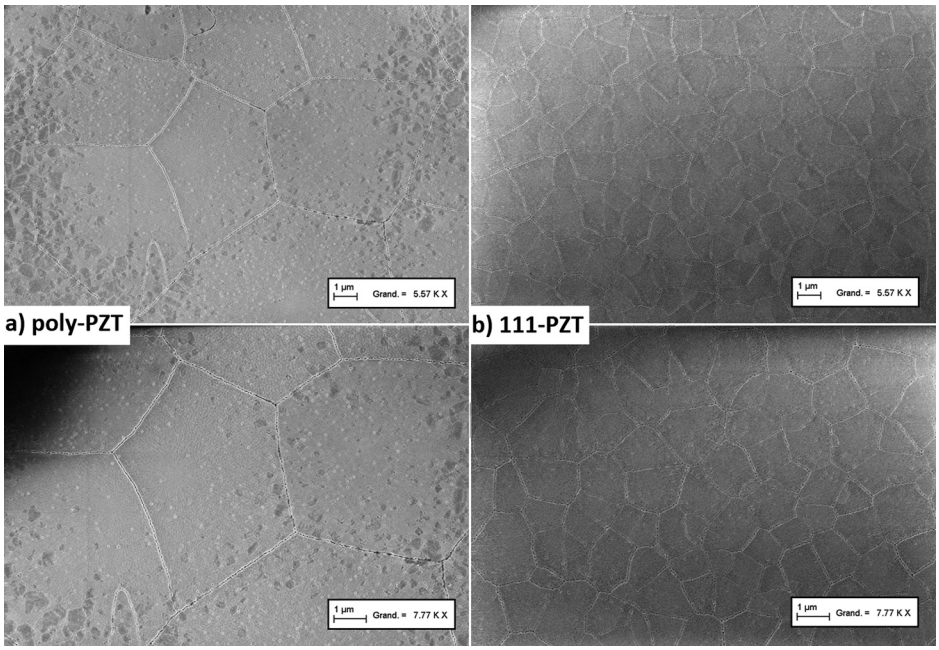

FIG. 8. SEM top view on PZT layers. (a) polycrystalline-PZT: grains sizes are about 10 μm and (b) (111)-PZT films, grains sizes are typically 1–2 μm.

Figure 4. Thus, the starting point is the same for any V_{DC}. The static dielectric permittivity ε_S is bounded by [1; 1000], the central relaxation times τ is bounded by $[0, (2\pi 50 \times 10^9)^{-1}]$, the broadening α is free to act on its maximum range [0; 1] and finally, ε_∞ is bounded by [1; 5]. The real part ε'_{C-C} and imaginary part ε''_{C-C} are presented on Figure 7(a) on a logarithmic frequency axis from 1 GHz up to 10 THz.

For readability purpose, only a few results were selected for their relevance. The dotted lines denote the already discussed experimental data of Figure 4 and which served to the fitting procedure. The continuous lines symbolize the *Cole-Cole* fitting results. Table II summarizes the set of *Cole-Cole* parameters for some electric field values.

According to these results and in both cases (111-PZT and polycrystalline-PZT), the central relaxation time appears to be similar and close to 2 ps for low V_{DC} values. When V_{DC} reaches its maximum value, this relaxation time is divided by 4 (see Figure 7(b)). One can note that α is quasi constant whatever V_{DC} is. Nevertheless, it is interesting to observe a significant shift between $\alpha_{(111)}$ and $\alpha_{(poly)}$. Then, a larger relaxation times distribution is observed in the case of 111-PZT case. This result could be directly related to the micro-structure of the film as we can see on Figure 8.

Actually, from the SEM photography, we note that for (111) and polycrystalline films, the grain sizes are completely different. Typically, a size of 1–2 μm for (111)-PZT film and about 10 μm for polycrystalline film is observed. Note that as the gap in the coplanar lines is in the order of 1 μm, the electromagnetic wave is very sensitive to the micro-structure of the films.

Finally, from these results, the V_{DC} dependence of the relaxation time is reminiscent of the Arrhenius law which relates relaxation time and temperature. Thus, it is tempting to write like already proposed by Glinchuk *et al.*[13]

$$\tau \approx \tau_0 e^{\left(\frac{U-\varphi(E_{ext}+E_{int})}{k_B T}\right)}, \tag{3}$$

where τ_0 is a pre-factor, U is the barrier height between different dipole orientations, φ is a normalization coefficient, k_B is the Boltzmann's constant, T is the absolute temperature, E_{ext} the energy provided by external voltage source, and E_{int} denotes the internal energy of the ferroelectric material under test.

V. CONCLUSION

In this paper, we have presented a complete characterization of (111)-oriented (using TiO_x buffer layer) and polycrystalline $Pb(Zr,Ti)O_3$ thin films grown on Al_2O_3 substrates by RF-magnetron sputtering. The microwave properties of

the films were evaluated using a two-dimensional vector finite element method in a large frequency range [1 GHz–67 GHz]. This work highlighted a very large dispersion of the relative permittivity with a maximum value of 0.7%/GHz when DC field is approximately 30 kV/cm and 0.4%/GHz when DC field reaches its maximum value of 235 kV/cm. The losses tangent exceeded 50% at 60 GHz without applied DC field and decreases to 27% for maximum applied DC field. The tunability was close to 60% at 1 GHz and reaches 47% at 67 GHz. Then, the result of the full wave analysis was fitted using a dielectric relaxation approach. The *Cole-Cole* relaxation model appeared as the simplest model able to meet our experimental needs. To the best of the author knowledge, it is the first time, in thin film form, that the relaxation time and its dependence with the applied electric field are determined. An experimental interval for the optical dielectric permittivity ε_∞ was determined by using spectroscopic ellipsometer in the 0.75–4.75 eV photon energy region. Through this relaxation function, it appeared that the central relaxation time was close to 2 ps when no external electric field was applied and reaches 0.6 ps under a DC field of 235 kV/cm. This result was similar for the both samples (111-PZT and polycrystalline-PZT). Nevertheless, a significant shift between the distributions broadening $\alpha_{(111)}$ and $\alpha_{(poly)}$ is observed. The methodology developed in this study is applicable to a wide class of materials in thin film form.

[1]P. Muralt, R. G. Polcawich, and S. Trolier-McKinstry, "Piezoelectric thin films for sensors, actuators, and energy harvesting," MRS Bull. **34**, 658–664 (2009).
[2]S. Trolier-McKinstry and P. Muralt, J. Electroceram. **12**, 7–17 (2004).
[3]L. L. Sun, O. K. Tan, and W. G. Zhu, J. Appl. Phys. **99**, 094108 (2006).
[4]J. F. Scott, Science **315**, 954 (2007).
[5]J. C. Booth, R. H. Ono, I. Takeuchi, and K.-S. Chang, Appl. Phys. Lett. **81**, 718 (2002).
[6]S. S. Gevorgian and E. L. Kollberg, IEEE Trans. MTT **49**(11), 2117–2124 (2001).
[7]I. Vendik, O. Vendik, V. Pleskachev, A. Svishchev, and R. Wordenweber, IEEE MTT-S Int. Microwave Symp. Dig. **3**, 1461–1464 (2001).
[8]N. Setter, D. Damjanovic, L. Eng, G. Fox, S. Gevorgian, S. Hong, A. Kingon, H. Kohlstedt, N. Y. Park, G. B. Stephenson, I. Stolitchnov, A. K. Taganstev, D. V. Taylor, T. Yamada, and S. Streiffer, J. Appl. Phys. **100**, 051606 (2006).
[9]L. M. Sanchez, D. M. Potrepka, G. R. Fox, I. Takeuchi, K. Wang, L. A. Bendersky, and R. G. Polcawich, J. Mater. Res. **28**, 1920–1931 (2013).
[10]C. Elissalde and J. Ravez, J. Mater. Chem. **11**, 1957 (2001).
[11]A. Peláiz-Barranco and J. D. S. Guerra, Mater. Res. Bull. **45**, 1311–1313 (2010).
[12]H. Hassan, M. Maglione, M. D. Fontana, and J. Handerek, J. Phys.: Condens. Matter **7**, 8647–8654 (1995).
[13]M. D. Glinchuk and V. A. Stephanovich, J. Appl. Phys. **85**(3), 1722 (1999).
[14]P. Debye, *Polar Molecules, Chemical Catalogue Company*, New York (1929).
[15]K. S. Cole and R. H. Cole, J. Chem. Phys. **9**, 341 (1941).
[16]F. Ponchel, J.-F. Legier, C. Soyer, D. Rémiens, J. Midy, T. Lasri, and G. Guégan, Appl. Phys. Lett. **96**, 252906 (2010).
[17]F. Ponchel, J. Midy, J.-F. Legier, C. Soyer, D. Rémiens, T. Lasri, and G. Guégan, J. Appl. Phys. **107**, 054112 (2010).
[18]F. Ponchel, X. Lei, D. Rémiens, G. Wang, and X. Dong, Appl. Phys. Lett. **99**, 172905 (2011).
[19]P. Muralt, T. Maeder, L. Sagalowicz, S. Hiboux, S. Scalese, D. Naumovic, R. G. Agostino, N. Xanthopoulos, H. J. Mathieu, L. Patthey, and E. L. Bullock, J. Appl. Phys. **83**, 3835 (1998).
[20]B. Vilquin, R. Bouregba, G. Poullain, M. Hervieu, and H. Murray, Eur. Phys. J. Appl. Phys. **15**, 153–165 (1999).
[21]N. Sama, R. Herdier, D. Jenkins, C. Soyer, D. Remiens, M. Detalle, and R. Bouregba, J. Cryst. Growth **310**, 3299–3302 (2008).
[22]D. Nuzhnyy, J. Petzelt, I. Rychetsky, and G. Trefalt, Phys. Rev. B **89**, 214307 (2014).
[23]L. Pintilie, I. Vrejoiu, D. Hesse, G. LeRhun, and M. Alexe, Phys. Rev. B **75**, 224113 (2007).
[24]H. Lee, Y. S. Kang, S.-J. Cho, B. Xiao, H. Morkoç *et al.*, J. Appl. Phys. **98**, 094108 (2005).